

where σ'_0 is the mean effective confining pressure; a is a coefficient -function of void ratio- which is modified in Figure. 8 to fit the shear wave velocity measurements. The coefficient a varies with density, as shown in Fig. 8. The coefficient of lateral stress, $K_0 = \sigma'_h / \sigma'_v$ (where σ'_h and σ'_v are horizontal and vertical effective stress, respectively) was introduced to calculate the mean effective confining pressure, σ'_0 ,

$$\sigma'_0 = \frac{1+2K_0}{3} \sigma'_{v0} \quad (2)$$

Herein, K_0 is determined with Eq. (3) (Jaky, 1944)

$$K_0 = 1 - \sin \varphi \quad (3)$$

where φ is the internal friction angle ($35^\circ - 38^\circ$), determined by El-Sekelly et al. (2014) for similar Ottawa sand with relative density of 45% and 80% using direct shear test.

The comparison results in Figure. 8 demonstrate that the measured shear wave velocities follow the same trend of Eq. (1) (Hardin and Richart, 1963).

Also, the measured ratio in Figure. 8, $V_{s,80}/V_{s,45} = 190/166.5 = 1.14$. This ratio is compared with Hardin and Richart (1963) and Seed and Idriss (1970) correlation.

According to the prediction by Hardin and Richart Ottawa correlation for G_{\max} of rounded sand (Hardin and Richart, 1963):

$$G_{\max} = \frac{2630(2.17-e)^2}{1+e} \sqrt{\sigma'_0} \quad (\text{psi}) \quad (4)$$

So, for the same σ'_0 :

$$\frac{G_{\max 80}}{G_{\max 45}} = \frac{(2.17-e_{80})^2}{(2.17-e_{45})^2} \cdot \frac{1+e_{45}}{1+e_{80}} \quad (5)$$

Where $e_{80}=0.53$; $e_{45}=0.62$. Therefore,

$$\frac{G_{\max 80}}{G_{\max 45}} = \frac{(2.17-0.53)^2}{(2.17-0.62)^2} \cdot \frac{1+0.62}{1+0.53} = 1.185 \quad (6)$$

But,

$$G_{\max} = \rho V_s^2 \Rightarrow V_s = \sqrt{\frac{G_{\max}}{\rho}} = \sqrt{\frac{G_{\max} \cdot g}{(\rho \cdot g)_{\text{sat}}}} \quad (7)$$

$$(\rho \cdot g)_{\text{sat}} = \frac{G+e}{1+e} (\rho \cdot g)_{\text{water}} \quad (8)$$

Using $G = 2.65$ for specific gravity.

$$(\rho \cdot g)_{\text{sat}} = \frac{2.65+e}{1+e} (\rho \cdot g)_{\text{water}} \quad (9)$$

$$\frac{(\rho \cdot g)_{\text{sat 80}}}{(\rho \cdot g)_{\text{sat 45}}} = \frac{2.65+e_{80}}{2.65+e_{45}} \cdot \frac{1+e_{45}}{1+e_{80}} \quad (10)$$

So,

$$\frac{V_{s80}}{V_{s45}} = \sqrt{\frac{G_{\max 80}}{G_{\max 45}} \cdot \frac{(\rho \cdot g)_{\text{sat 45}}}{(\rho \cdot g)_{\text{sat 80}}}} = \sqrt{(1.185) \cdot \frac{2.65+e_{45}}{2.65+e_{80}} \cdot \frac{1+e_{80}}{1+e_{45}}} \quad (11)$$

$$\frac{V_{s80}}{V_{s45}} = \sqrt{(1.185) \cdot \frac{2.65+0.62}{2.65+0.53} \cdot \frac{1+0.53}{1+0.62}} = \sqrt{1.185 \cdot 1.03 \cdot 0.94} = 1.07 \tag{12}$$

According to the prediction by Seed and Idriss (1970) correlation of Gmax versus Dr:

$$G_{max} = 1000K_{2max} \sqrt{\bar{\sigma}_0} \tag{13}$$

($\bar{\sigma}_0$ and in G_{max} psi)

Table 1 Values of K_{2max} (Seed and Idriss, 1970)

$D_r(\%)$	K_{2max}
45	9.4
80	14.0

K_{2max} values for $D_r = 80\%$ is obtained by linear interpolation based on Table 1.

So, for the same $\bar{\sigma}_0$:

$$\frac{G_{max80}}{G_{max45}} = \frac{14.0}{9.4} = 1.489 \tag{14}$$

And

$$\frac{V_{s80}}{V_{s45}} = \sqrt{\frac{G_{max80}}{G_{max45}} \cdot \frac{2.65 + e_{45}}{2.65 + e_{80}} \cdot \frac{1 + e_{80}}{1 + e_{45}}} = \sqrt{1.489 \cdot 1.03 \cdot 0.94} = 1.20 \tag{15}$$

Thus, the experimental ratio of: $\frac{V_{s80}}{V_{s45}} = 1.14$ is consistent with the range of ratios, 1.07-1.20, obtained from the Hardin and Richart (1963) and Seed and Idriss (1970) correlation.

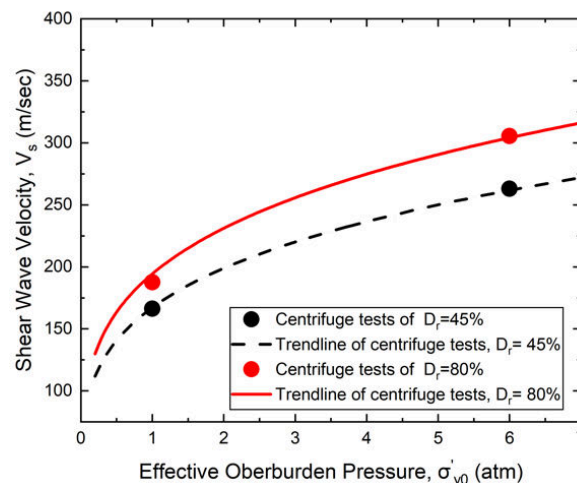


Figure 8. measured shear wave velocities of centrifuge tests and the corresponding trendlines

CONCLUSION

A series of four centrifuge tests (Tests 45-1, 45-6, 80-1 and 80-6) with different relative densities and effective overburden pressures were conducted in order to study the sand behavior under low and high confining pressures. Some of the experimental results were analyzed and

demonstrated. A new centrifuge technique was established to provide sand model with various confining pressures with three distinct layers: the saturated sand deposit, the transition layer and the heavy lead shot layer. This technique proved successful and opens new venues for research at any centrifuge facility. According to the data analysis, amplification of acceleration was observed under low confining pressure in Test 45 - 1 and Test 80 - 1, while de-amplification of acceleration existed in Test 45 - 6 and Test 80 - 6 under high confining pressures. The shear wave velocities measured from bender elements for loose and dense sand models were in good agreement with the formula form of $V_s = a(\sigma'_0)^{0.25}$, also validated by literature predictions.

REFERENCES

- Andrus, R. D., and Stokoe II, K. H. (2000). "Liquefaction resistance of soils from shear-wave velocity." *Journal of geotechnical and geoenvironmental engineering*, ASCE, 126(11), 1015-1025.
- Boulanger, R. W., and Idriss, I. M. (2004). "State normalization of penetration resistance and the effect of overburden stress on liquefaction resistance." *Proceedings 11th SDEE and 3rd ICEGE*, University of California, Berkeley, CA.
- Boulanger, R. W., Wilson, D. W. and Idriss, I. M. (2011). "Examination and reevaluation of SPT-based liquefaction triggering case histories." *Journal of geotechnical and geoenvironmental engineering*, ASCE, 138(8), 898-909.
- Boulanger, R. W., and Idriss, I. M. (2012). "Probabilistic standard penetration test-based liquefaction-triggering procedure." *Journal of geotechnical and geoenvironmental engineering*, ASCE, 138(10), 1185-1195.
- Cetin, K. O., Seed, R. B., Der Kiureghian, A., Tokimatsu, K., Harder Jr, L. F., Kayen, R. E., and Moss, R. E. (2004). "Standard penetration test-based probabilistic and deterministic assessment of seismic soil liquefaction potential." *Journal of geotechnical and geoenvironmental engineering*, ASCE, 130(12), 1314-1340.
- Chen, L., Hou, L., Cao, Z., Yuan, X., Sun, R., Wang, W., ... & Dong, L. (2008). "Liquefaction investigation of Wenchuan earthquake." *14th World Conf. on Earthquake Engineering*.
- Dobry, R., and T. Abdoun. "3rd Ishihara Lecture: An investigation into why liquefaction charts work: A necessary step toward integrating the states of art and practice." *Soil Dynamics and Earthquake Engineering* 68 (2015): 40-56.
- El-Sekelly, W., Tessari, A., and Abdoun, T. (2014). "Shear wave velocity measurement in the centrifuge using bender elements." *Geotechnical Testing Journal*, 37(4), 689-704.
- Gillette, D. (2013). "Liquefaction issues for dam safety - Bureau of Reclamation." *Presentation in One-Day Workshop, Committee on State of the Art and Practice in Earthquake Induced Soil Liquefaction Assessment*, National Research Council of the National Academies, Washington, DC, November 12.
- Hardin, B. O., and Richart Jr., F. E. (1963). "Elastic wave velocities in granular soils." *J. Soil Mech. Found. Div.*, ASCE, 89(1), 33-65.
- Huang, Y., & Yu, M. (2013). "Review of soil liquefaction characteristics during major earthquakes of the twenty-first century." *Natural hazards*, 65(3), 2375-2384.
- Hynes, M. E., Olsen, R. S., and Yule, D. E. (1999). "Influence of confining stress on Liquefaction Resistance." *Proc., Int. Workshop on Phys. and Mech. of Soil Liquefaction*, Balkema, Rotterdam, The Netherlands, 145-152.
- Idriss, I. M., and Boulanger R. W. (2006). "Semi-empirical procedures for evaluating

- liquefaction potential during earthquakes." *Soil Dynamics and Earthquake Engineering*, 26(2-4), 115-130.
- Idriss, I. M., and Boulanger, R. W. (2008). "Soil liquefaction during earthquakes." Monograph MNO-12, Earthquake Engineering Research Institute, Berkeley, CA.
- Idriss, I. M., and Boulanger, R. W. (2010). "SPT-based liquefaction triggering procedures." Report UCD/CGM-10/02, Dept. of Civil and Environmental Engineering, Univ. of California, Davis, CA.
- Jaky, J. (1944). "The coefficient of earth pressure at rest." *J. Soc. Hung. Eng. Arch. (Magyar Mernok es Epitesz-Egyelet Kozlonye)*, 355–358.
- Joseph, P. G., Einstein, H. H., and Whitman, R. V. (1988). "A literature review of geotechnical centrifuge modeling with particular emphasis on rock mechanics." MIT Report to the Air Force Engineers and Service Center, Accession No. ADA213793, Tyndall Air Force Base, FL.
- Robertson, P. K., and Wride, C. E. (1998). "Evaluating cyclic liquefaction potential using the cone penetration test." *Canadian Geotechnical Journal*, 35(3), 442-459.
- Seed, H. B. "Earthquake-resistant design of earth dams." Proc., Symp. Seismic Des. of Earth Dams and Caverns, ASCE, New York, (1983) 41–64.
- Seed, H. B., and Idriss, I. M. (1970). "Analyses of ground motions at Union Bay, Seattle during earthquakes and distant nuclear blasts." *Bulletin of the Seismological Society of America*, 60(1), 125-136.
- Seed, H. B., and I. M. Idriss. "Simplified procedure for evaluating soil liquefaction potential." *Journal of Soil Mechanics & Foundations Div* (1971).
- Sharp, M. K., Dobry, R., & Abdoun, T. (2003). "Liquefaction Centrifuge Modeling of Sands of Different Permeability." *Journal of geotechnical and geoenvironmental engineering*, 129(12), 1083-1091.
- Taylor, R. N. (1995). "Centrifuges in modelling: principles and scale effects." Chapter 2, *Geotechnical centrifuge technology*, R. N. Taylor, ed., Blackie Academic & Professional, London, 19-33.
- Youd, T. L., and Idriss, I. M. (2001). "Liquefaction resistance of soils: summary report from the 1996 NCEER and 1998 NCEER/NSF workshops on evaluation of liquefaction resistance of soils." *Journal of geotechnical and geoenvironmental engineering*, ASCE, 127(4), 297-313.

Numerical Investigation of Geophysical Measurements for Liquefaction Triggering Evaluation in Soils Exhibiting Natural Spatial Variability

Joseph T. Coe, Ph.D.¹; Siavash Mahvelati, Ph.D.²; and Alireza Kordjazi, Ph.D.³

¹Associate Professor, Dept. of Civil and Environmental Engineering, Temple Univ., Philadelphia, PA. E-mail: joseph.coe@temple.edu

²Vibra-Tech Engineers, Hazleton, PA. E-mail: siavashm@vibratechinc.com

³Graduate Research Assistant, Dept. of Civil and Environmental Engineering, Temple Univ., Philadelphia, PA. E-mail: alireza.kordjazi@temple.edu

ABSTRACT

One of the first steps in assessment of liquefaction hazards consists of evaluating the potential for liquefaction triggering at a site. Procedures based on the standard penetration test (SPT) and cone penetration test (CPT) are often used. However, geophysical measurements of shear wave velocity (V_s) have also been used to evaluate liquefaction triggering since V_s is a proxy for soil stiffness. Measurements of V_s for these triggering evaluations are often acquired using downhole methods (e.g., seismic CPT or P-S suspension logging) or cross-hole methods. SPT, CPT, and borehole-based geophysical measurements provide data in the localized region surrounding the boreholes. This presents challenges when attempting to evaluate liquefaction triggering in natural soils that exhibit spatial stiffness variability. Recently, surface wave measurements have grown in popularity for geotechnical investigations and have been used to evaluate V_s profiles for liquefaction triggering analysis. However, surface wave methods typically apply wavefield transformations to evaluate dispersion characteristics. This essentially introduces a form of spatial averaging that can lead to uncertainty in V_s measurements when soils exhibit appreciable spatial variability along the survey line. One promising development in surface wave testing involves the use of full waveform inversion (FWI). FWI attempts to match the entirety of each recorded signal rather than a dispersion curve derived from the corresponding wavefield transformation. Therefore, FWI has the potential to offer broad spatial coverage while avoiding the inherent limitations of a dispersion-based surface wave approach. In this study, numerical modeling was performed to simulate wave propagation in soils exhibiting natural spatial variability. Comparisons were made regarding the extent to which different geophysical approaches could reliably estimate liquefaction triggering. The results demonstrated that FWI can outperform downhole/cross-hole measurements and a dispersion-based surface wave approach when implementing V_s -based liquefaction triggering procedures in spatially variable soil conditions.

INTRODUCTION

Liquefaction refers to loose, cohesionless, saturated soils losing their strength in response to dynamic loading. Excess pore water pressures develop when water cannot escape the voids as the soil attempts to contract in response to rapid loading. Liquefaction occurs when the effective stress reduces to zero in response to the excess pore pressure buildup. The strength loss and any post-liquefaction settlements from subsequent excess pore pressure dissipation can cause significant ground deformation as highlighted in recent notable seismic events such as the 2010 M_w 7.0 Darfield, 2011 M_w 6.2 Christchurch, and 2015 M_w 7.8 Gorkha earthquakes. Because of the potential damage caused by liquefaction, a significant amount of research has explored

several aspects of its occurrence, including susceptibility (Chung and Rogers 2017), effects on infrastructure (Turner et al. 2016), and mitigation (Stuedlein et al. 2016).

Considerable research on liquefaction triggering has continued since seminal efforts after the 1964 Mw 7.6 Niigata and 1964 Mw 9.2 Great Alaskan earthquakes (e.g., Seed and Idriss 1971; Seed et al. 1985; Robertson and Wride 1998; Idriss and Boulanger 2008; Boulanger and Idriss 2014). These efforts resulted in a simplified approach that computes a factor of safety (FS_L) by comparing soil resistance [i.e., cyclic resistance ratio (CRR)] to the stresses imparted by vertically propagating shear waves [i.e., cyclic stress ratio (CSR)]:

$$CSR_{M=7.5}(z) = CSR_{M=m}(z) \cdot \frac{1}{MSF} = 0.65 \cdot \frac{\left(\frac{PGA}{g}\right) \cdot \sigma'_{vo}(z) \cdot r_d}{\sigma'_{vo}} \cdot \frac{1}{MSF} \quad (1)$$

where z is the depth, σ'_{vo} is the initial vertical effective stress, σ_{vo} is the initial vertical total stress, PGA is the peak horizontal ground acceleration, g is the acceleration due to gravity, r_d is a depth-dependent stress reduction coefficient, and MSF is a magnitude scaling factor for a reference earthquake magnitude $M = 7.5$. CRR has typically been calibrated against liquefaction case histories (e.g., Kayen et al. 2013; Boulanger and Idriss 2014). CRR is typically computed from corrected SPT blow count $[(N_1)_{60}]$, corrected CPT tip resistance (q_{c1N}), and small-strain geophysical estimates of V_s . A typical liquefaction triggering analysis estimates CSR with depth (Eq. 1) and CRR from in situ parameters. The FS_L is subsequently computed and specific zones can be targeted for mitigation efforts. A probabilistic approach can also estimate a probability of liquefaction (P_L) using a statistical analysis based on Bayesian updating (e.g., Kayen et al. 2013).

One aspect of liquefaction that has increasingly received attention is the role of spatial variability of soil deposits caused by ongoing geologic, environmental, and physical-chemical processes that lead to fluctuations in their in situ properties (Phoon and Kulhaway 1999). This variability can cause uncertainty when evaluating liquefaction triggering because CRR is based on in situ soil parameters. A number of recent research efforts have attempted to quantify the effects of spatial variability on liquefaction (Popescu et al. 2005, Baker and Faber 2008, Montgomery and Boulanger 2016; Bong and Stuedlein 2018). However, the majority of efforts have focused on penetration resistances from SPT/CPT, which are localized measurements. These measurements may prove insufficient to quantify the extent of liquefaction triggering unless a cost-prohibitive number of site locations are tested.

Geophysical methods can provide rapid spatial assessment of liquefaction resistance based on V_s - CRR relationships. However, absent in the literature is discussion of the effectiveness of various geophysical methods for this purpose. For example, borehole measurements from downhole seismic (DS) testing or crosshole tomography (CT) exhibit similar limitations as SPT/CPT related to the localized nature of their measurements. Surface wave methods such as multichannel analysis of surface waves (MASW) suffer from limitations related to the wavefield transformations used to convert the signals into dispersion information (e.g., phase velocity versus frequency). In fact, the presence of spatial variability can create artifacts that complicate selection of an appropriate dispersion curve. Additionally, the forward modeling used to compute theoretical dispersion curves during inversion assumes uniform, contiguous strata. Lateral stiffness variability is subsequently spatially-averaged into a one-dimensional (1D) V_s profile assumed to represent the conditions beneath the receiver array center.

A full waveform inversion (FWI) tomographic approach can potentially address the aforementioned issues with current geophysical methods for liquefaction triggering assessment in spatially variable soils. In FWI tomography, an earth model is constructed by iteratively

matching the entirety of waveforms observed at various locations (typically from surface receivers). The amount of misfit between synthetic waveforms from forward modeling and the observed waveforms is compared until a convergence criterion is met. This iterative inversion process results in a high resolution image of the subsurface. FWI has recently been applied for geotechnical site characterization to evaluate the presence of near-surface anomalous conditions (e.g., Fathi et al. 2016; Nguyen and Tran 2018; Mahvelati and Coe 2019). The purpose of this paper is to evaluate the effectiveness with which FWI tomography can measure liquefaction triggering spatial variability and to compare FWI to borehole geophysical (DS and CT) and surface wave (2D MASW) measurements. This was accomplished by simulating wave propagation in a domain generated using random field theory (RFT) (VanMarcke 1984) with spatial variability associated with typical geologic materials.

EXPERIMENTAL APPROACH

The domain for this study was developed using the same MATLAB[®] script from Montgomery and Boulanger (2016). The script applies a Gaussian correlation function to generate a spatially-correlated random field model (RFM) through lower-upper (LU) decomposition of the covariance matrix. The domain is 10.0 m deep and 80.0 m wide and contains a single alluvial sandy soil with an average $V_S = 200$ m/s (Fig. 1). The coefficient of variation (COV) for V_S was set to 30%, which is consistent with in situ properties of coarse-grained alluvial soils (e.g., Phoon and Kulhawy 1999). The spatial extent of variability along the vertical and horizontal directions were set to $\theta_z = 0.5$ m and $\theta_x = 10.0$ m, which is consistent with previous studies (e.g., Phoon and Kulhawy 1999; Montgomery and Boulanger 2016). The ground water table was located at $z_w = 1.0$ m, below which the P-wave velocity (V_P) was fixed at 1500 m/s. Above the water table, V_P was derived from V_S based on an assumed Poisson's ratio (ν) equal to 0.2. The mass density (ρ) of the soil was subsequently estimated using the Burns and Mayne (1996) relationship:

$$\rho \left(\frac{\text{g}}{\text{cm}^3} \right) = 0.277 + 0.648 \log V_S \left(\frac{\text{m}}{\text{s}} \right) \quad (2)$$

Once the V_S , V_P , z_w , and ρ were defined, σ'_{vo} and σ_{vo} were computed and the Kayen et al. (2013) approach was used to estimate the depth-dependent CSR and CRR:

$$CRR = exp$$

$$\left\{ \frac{\left[(0.0073 \cdot V_{S1})^{2.8011} - 2.6168 \cdot \ln M - 0.0099 \cdot \ln \sigma'_{vo} + 0.0028 \cdot FC - 0.4809 \cdot \Phi^{-1}(P_L) \right]}{1.946} \right\} \quad (3)$$

$$V_{S1} = C_{V_S} \cdot V_S = \left(\frac{P_a}{\sigma'_{vo}} \right)^{0.25} \cdot V_S \quad (4)$$

where Φ^{-1} is the complementary cumulative distribution function for a probability of liquefaction (P_L), FC is the fines content correction factor, V_{S1} is the normalized V_S , C_{V_S} is the overburden correction factor, and $P_a = 1$ atm. A deterministic evaluation was performed, for which Kayen et al. (2013) recommends $P_L = 15\%$ in Eq. 3 and $FS_L = 1.17$ as the boundary for triggering. CSR was computed using a $PGA = 0.3g$ for a $M = 7.5$ event. In addition to the domain in situ parameters, Fig. 1 presents the results from Eqs. 1 and 3 – 4 for CSR , CRR , and FS_L .

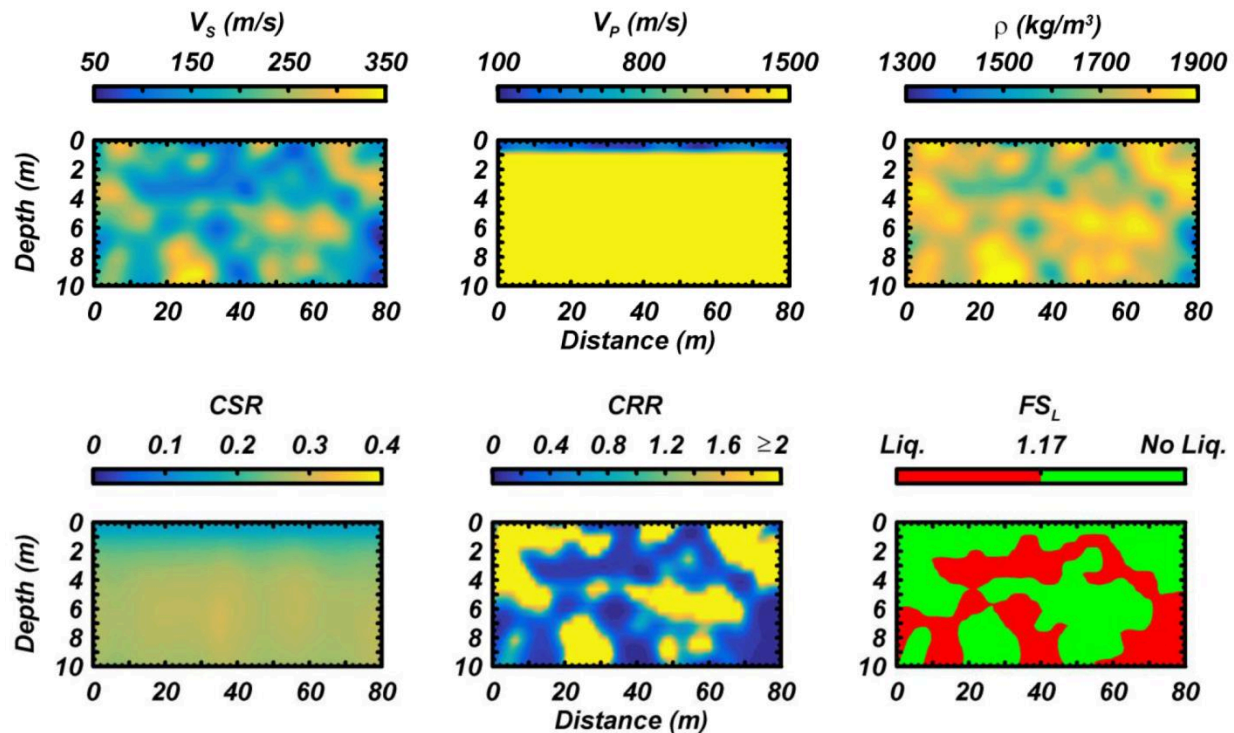


Figure 1. RFM domain used in this study, including V_S , V_P , ρ , CSR , CRR , and FS_L .

Wave propagation was modeled using the SPEC2D code, which uses the spectral element method (SEM). SEM formulates the equations of motion using the weak form similar to the finite element method (FEM) but with higher degree basis functions (Tromp et al., 2008). This combined with the nodal interpolation scheme yields a diagonal mass matrix that simplifies inversion and improves parallelization. SEM has been used in numerous studies to simulate wave propagation across a range of scales (e.g., Komatitsch and Tromp 1999; Virieux and Operto 2009; Kordjazi et al. 2018). A stress-free boundary condition was specified for the top surface to ensure the development of surface waves. Additionally, the other boundaries were subjected to Clayton-Engquist-Stacey absorbing conditions to ensure that outgoing waves were not reflected back into the domain (Stacey 1988).

Forward modeling was used to generate synthetic waveforms for: (1) 2D MASW; (2) DS; (3) CT; and (4) “observed” waveforms for FWI. Figure 2 illustrates the workflow for each method. For MASW, a 48 channel linear array with 0.5 m receiver spacing (dx) was placed on the ground surface (total array length of 23.5 m). A 30 Hz Ricker wavelet source was placed at a source offset (SO) of 10.0 m from the first channel (i.e., $20dx$). The midpoint of the first array was centered at $x = 22.25$ m and the entire array was shifted by 0.5 m until the last array receiver reached the edge of the model at $x = 79.5$ m. This resulted in 92 recordings, which were transformed into dispersion images within the Geometrics SeisImager/SW[®] software package. Fundamental-mode dispersion curves were extracted from each of the dispersion images and inverted using a local search algorithm with a non-linear least squares approach to compute the dispersion misfit. The inversion iterations were discontinued once the root-mean-square (RMS) error for the dispersion misfit was 5%. The resulting 92 1D V_S profiles were then linearly interpolated in the x and z directions to create a 2D V_S profile.

Borehole geophysical testing was simulated using a total of eight boreholes spaced equally at 10.0 m across the domain (from $x = 5.0$ m - 75.0 m). Each borehole spanned the 10.0 m depth of

the domain. This configuration yielded seven CT datasets from borehole pairs. 30 Hz Ricker wavelet sources were located at 0.5 m intervals in each source borehole and a constant spacing of 0.25 m was used for the receivers. The first source/receiver was located at $z = 0.25$ m and the last one was at $z = 9.75$ m. This configuration resulted in 20 sources and 39 receivers per borehole pair. To solve the CT inversion, a ray-tracing scheme was required to determine the ray paths (Giroux and Larouche 2013) (Fig. 2). In this study, a shortest-path method was used to compute the travel-time based on Fermat’s principle. To increase the accuracy and provide adequate angular coverage, the domain was discretized using cells with primary nodes at their corners together with five secondary nodes along cell edges (Giroux and Larouche 2013). The open-source pyGIMLi package (Rücker et al. 2017) was used to perform the CT analysis.

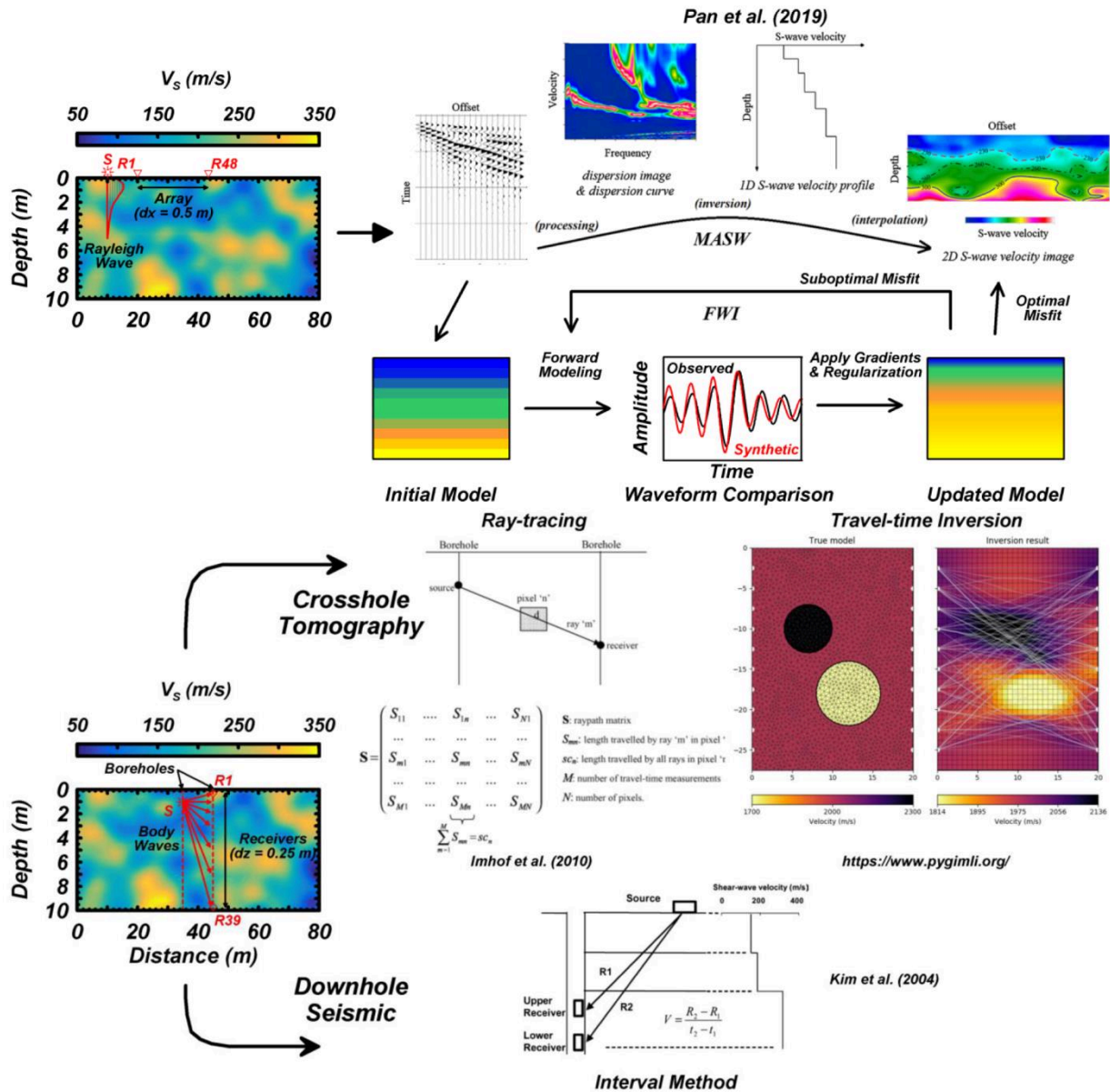


Figure 2. Schematics of workflows for MASW, FWI, CT, and DS.

The same receiver configuration was used in each borehole for DS testing (Fig. 2). However,

only two 30 Hz Ricker wavelets were used as surface sources located 2.0 m on either side of the borehole. This resulted in 16 sets of downhole datasets (i.e., two per borehole). The time interval method was used to estimate the average velocity between receiver measurements. This approach computed the V_S as the difference between the straight-line paths from the source to two receivers divided by their difference in shear wave arrival times. This analysis was performed using custom MATLAB® scripts. The two complementary V_S profiles were averaged for each borehole, resulting in eight 1D downhole V_S profiles. These 1D V_S profiles were linearly interpolated along the x direction to create a 2D V_S profile.

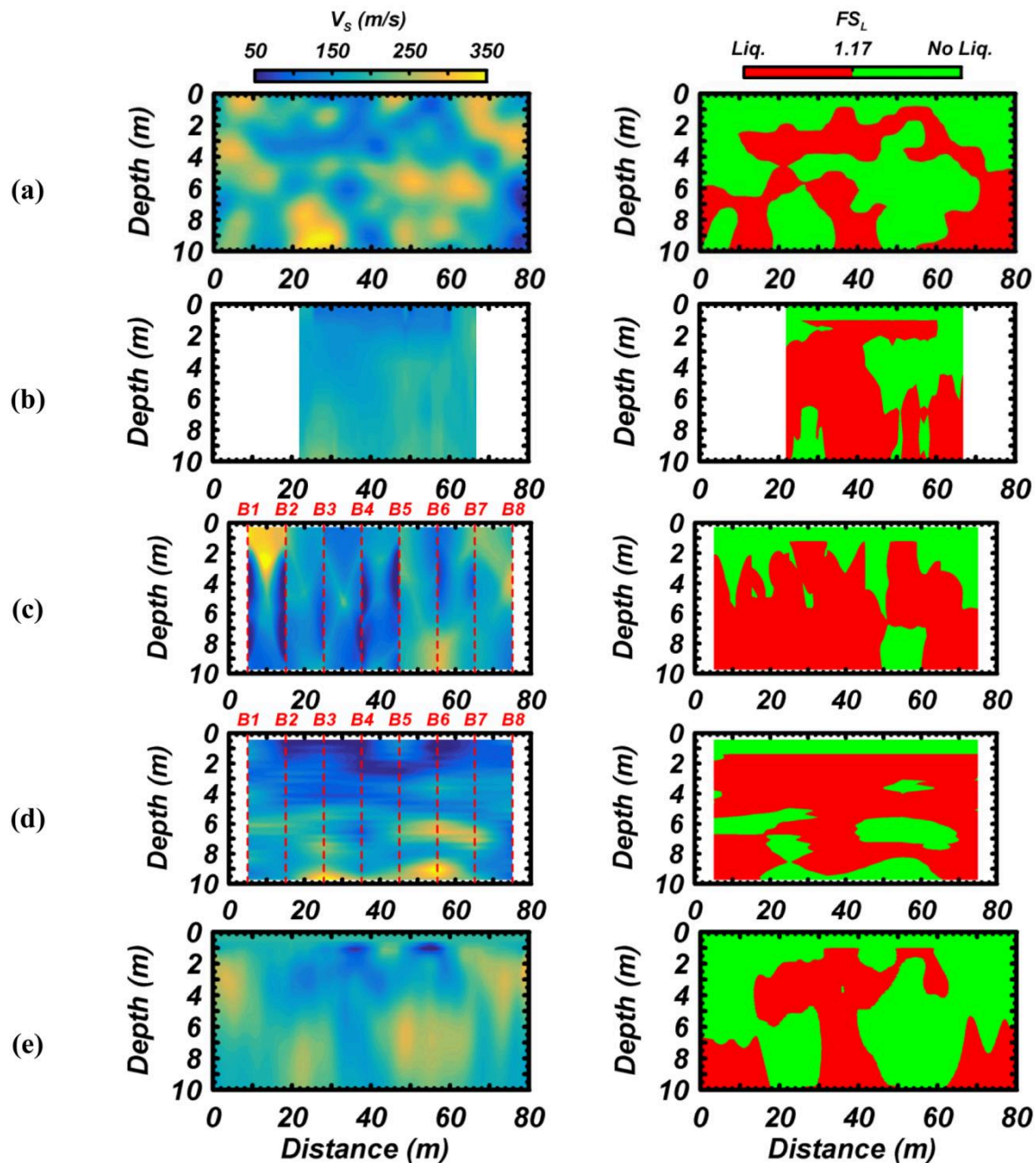


Figure 3. V_S and FS_L results: (a) True model; (b) 2D MASW; (c) CT; (d) DS; and (e) FWI.

Finally, FWI was performed using the seismic inversion software code SeisFlows (Mordak et